









Multiband superconductivity in strongly hybridized $1T'$ -WTe₂/NbSe₂ heterostructures

Wei Tao ¹, Zheng Jue Tong ¹, Anirban Das ^{2,3}, Duc-Quan Ho ¹, Yudai Sato,⁴ Masahiro Haze ⁴, Junxiang Jia ¹, Yande Que,¹ Fabio Bussolotti,⁵ K. E. Johnson Goh,^{1,5} BaoKai Wang,⁶ Hsin Lin,⁷ Arun Bansil,⁶ Shantanu Mukherjee,^{2,3,8} Yukio Hasegawa ⁴ and Bent Weber ^{1,9,*}

¹*Division of Physics and Applied Physics, School of Physical and Mathematical Sciences, Nanyang Technological University, Singapore 637371, Singapore*

²*Department of Physics, Indian Institute Of Technology Madras, Chennai, Tamil Nadu 600036, India*

³*Computational Materials Science Group IIT Madras Chennai, Tamil Nadu 600036, India*

⁴*The Institute for Solid State Physics, The University of Tokyo, 5-1-5 Kashiwa-no-ha, Kashiwa 277-8581, Japan*

⁵*Institute of Materials Research and Engineering, Agency for Science Technology and Research (A*STAR), 2 Fusionopolis Way, 08-03 Innovis, Singapore 138634, Singapore*

⁶*Department of Physics, Northeastern University, Boston, Massachusetts 02115, USA*

⁷*Institute of Physics, Academia Sinica, Taipei, Taiwan*

⁸*Quantum Centres in Diamond and Emergent Materials (QuCenDiem)-Group IIT Madras Chennai, Tamil Nadu 600036, India*

⁹*ARC Centre of Excellence for Future Low-Energy Electronics Technologies (FLEET), School of Physics, Monash University, Clayton VIC 3800, Australia*



(Received 24 July 2021; revised 8 March 2022; accepted 9 March 2022; published 24 March 2022)

The interplay of topology and superconductivity has become a subject of intense research in condensed-matter physics for the pursuit of topologically nontrivial forms of superconducting pairing. An intrinsically normal-conducting material can inherit superconductivity via electrical contact to a parent superconductor via the proximity effect, usually understood as Andreev reflection at the interface between the distinct electronic structures of two separate conductors. However, at high interface transparency, strong coupling inevitably leads to changes in the band structure, locally, owing to hybridization of electronic states. Here, we investigate such strongly proximity-coupled heterostructures of monolayer $1T'$ -WTe₂, grown on NbSe₂ by van der Waals epitaxy. The superconducting local density of states, resolved in scanning tunneling spectroscopy down to 500 mK, reflects a hybrid electronic structure well described by a multiband framework based on the McMillan equations which captures the multiband superconductivity inherent to the NbSe₂ substrate and that is induced by proximity to WTe₂, self-consistently. Our material-specific tight-binding model captures the hybridized heterostructure quantitatively and confirms that strong interlayer hopping gives rise to a semimetallic density of states in the two-dimensional WTe₂ bulk, even for nominally band-insulating crystals. The model further accurately predicts the measured order parameter $\Delta \simeq 0.6$ meV induced in the WTe₂ monolayer bulk, stable beyond a 2 T magnetic field. We believe that our detailed multiband analysis of the hybrid electronic structure provides a useful tool for sensitive spatial mapping of induced order parameters in proximitized atomically thin topological materials.

DOI: [10.1103/PhysRevB.105.094512](https://doi.org/10.1103/PhysRevB.105.094512)

I. INTRODUCTION

Inducing superconductivity by proximity in materials with nontrivial band topology [1–3] has become a method of choice in the search for unconventional forms of superconducting pairing [4,5]. Prominent examples are demonstrations of unconventional superconductivity in semiconductor nanowires with strong spin-orbit coupling [4], atomic chains and islands [5,6], as well as at the surfaces and edges of three-dimensional topological insulators [7] and semimetals [8]. At the one-dimensional (1D) edges of two-dimensional (2D) topological insulators [9,10], such as the quantum spin Hall (QSH) state [11], the presence of non-Abelian parafermions has been predicted [12].

In any material system, topologically trivial or nontrivial, the proximity effect can be understood in a microscopic picture to result from Andreev reflection of quasiparticles at the superconductor–normal-metal interface. The strength of the induced superconducting pairing is directly linked to the transparency of the interface, i.e., the tunneling coupling at the contact between the proximity-coupled materials. While strong induced pairing with a large order parameter may often be desired, e.g., to mitigate disorder or the effects of an applied magnetic field [4], it is often assumed that the tunnel-coupling does not induce any fundamental changes to the band structure. In stark contrast, exchange of charge, especially across atomically abrupt interfaces, can be expected to give rise to atomic bonding or at least perturbations of the electronic structure, which can lead to profound changes in the electronic band dispersion [13].

*b.weber@ntu.edu.sg

Here, we investigate the hybrid electronic structure of such strongly coupled heterostructures of the quantum spin Hall (QSH) candidate $1T'$ -WTe₂, grown by *in situ* van der Waals epitaxy on the type-II superconductor 2H-NbSe₂. Scanning tunneling spectroscopy down to 500 mK allows us to resolve the superconducting local density of states (LDOS), which we analyze within a self-consistent multiband framework based on the McMillan equations [14]. We show that superconductivity is induced in a semimetallic WTe₂ monolayer bulk, which we understand as a result of a strong interlayer tunneling across the heterointerface, leading to hybridization of electronic states. A material-specific mean-field tight-binding model is able to capture the hybrid electronic structure in the normal state, allowing direct quantitative comparison with the measured LDOS. As a result, our model is able to predict the magnitude of the induced superconducting order parameter, quantitatively, robust against magnetic fields beyond 2 T. Owing to strong hybridization, we observe a significant weakening of the topological edge state signature, measurable by an enhancement of the LDOS in the normal state at the edge, concomitant with a slight enhancement of the induced superconducting order parameter.

Tungsten ditelluride (WTe₂) and related members of the transition-metal dichalcogenide family with $1T'$ crystal structure have attracted much attention as candidate material systems to realize type-II Weyl [15] fermions and higher-order topology [16] in its three-dimensional (3D) bulk. Evidence of high-order semimetallic properties have recently been confirmed in superconducting Josephson junction measurements [17,18], showing that induced supercurrents are well localized to the materials' 1D edges ("hinges"). In atomic monolayers, a time-reversal-symmetry-protected 2D topologically insulating state [19] has been predicted, arising from inversion of the transition metal d and the chalcogen p orbitals, highly tunable by electric fields and strain [19]. While free-standing $1T'$ -WTe₂ monolayers had initially been predicted to be semimetallic with a negative fundamental band gap [19], a positive gap was later confirmed by density-functional theory and layer-dependent optical spectroscopy [20]. Quantum spin Hall insulating behavior and the presence of highly confined 1D metallic states at the edge have since been confirmed in electron transport [21,22], angle-resolved photoemission spectroscopy (ARPES), and scanning probe measurements [23,24] including microwave impedance microscopy [25]. However, the sensitivity of the WTe₂ band gap to strain [26] and electric fields [27] remains a matter of intense debate because significant variations in the magnitude and definition of the measured QSH bulk have been observed [20–24,27,28]. Recent reports indicate that the bulk gap observed may indeed arise from 2D electronic interactions [28], challenging the band-insulating picture [29,30].

The study of superconductivity remains of fundamental interest in both the QSH insulating [12,19,31] and semimetallic [32,33] states of $1T'$ -WTe₂, given theoretical predictions of nontrivial pairing. Intrinsic low-density superconductivity has recently been reported in the 2D bulk of electrostatically doped semimetallic WTe₂ monolayers [34,35], and is believed to be of nontrivial pairing [32,33]. Similarly, the 1D helical edge of any quantum spin Hall insulating state has

been predicted as a potential host for parafermions in the superconducting state [9,10,12,19,31].

Superconductivity up to relatively high critical temperatures and magnetic fields can be achieved by proximity coupling to a stable intrinsic superconductor, such as the layered type-II superconductor 2H-NbSe₂ ($T_C \simeq 7.2$ K, $B_{C2} \simeq 5$ T) [36–39]. Further to these studies, here we show that strong coupling to the superconductor gives rise to a hybrid multiband electronic structure, which needs to be taken into account when interpreting the detailed functional form of the induced superconducting local density of states.

II. RESULTS AND DISCUSSION

A. Crystal growth and atomic structure

Figure 1 shows scanning tunneling microscopy (STM) data of $1T'$ -WTe₂/2H-NbSe₂ heterostructures, grown by bufferless low-temperature van der Waals epitaxy. In agreement with previous studies of WTe₂ on bilayer graphene (BLG) [23,24], we observe Volmer-Weber growth of islands with disordered boundaries [Figs. 1(a) and 1(b)] and sizes up to a few tens of nanometer in diameter that are polycrystalline on NbSe₂ substrates. For this work, we focus on the intermediate coverage limit ($\approx 50\%$) in order to maximize the density of QSH edges, although nearly complete monolayers with coverage $>95\%$ can be achieved with reduced crystal quality.

Atomic-level detail of the WTe₂ lattice alignment with the substrate is shown in Figs. 1(d)–1(g) where we find that the respective chalcogen (Te and Se) sublattices align along the atomic rows of $1T'$ -WTe₂ (y direction). A 2D fast Fourier transform [Fig. 1(f)] of an area with $\approx 50\%$ WTe₂ monolayer coverage indeed confirms that the Bragg peaks of the WTe₂ and NbSe₂ lattices coincide within the accuracy of the measurement. We extract $a \simeq a_1 = 3.5 \pm 0.2$ Å, and $b \simeq 2a_2 \cos(30^\circ) = 6.2 \pm 0.3$ Å, in good agreement with the lattice parameters of WTe₂ ($a = 3.48$ Å and $b = 6.28$ Å) [20]. $a_1 = a_2 = 3.45$ Å are the lattice parameters of NbSe₂, local lattice matching would imply a 5% compressive lattice strain along b , which has previously been shown to further stabilize the WTe₂ bulk gap [26].

A first indication that we may expect strong hybridization in WTe₂/NbSe₂ heterostructures comes from a measurement of the monolayer height $h = 0.9 \pm 0.1$ nm, extracted from z -height distributions of large-scale topographic STM images (see Fig. 5, Appendix A), and is comparable to measurements of van der Waals stacked WTe₂/NbSe₂ ($h \simeq 0.7$ nm) [39]. The significantly lower layer height compared with WTe₂/BLG ($h \simeq 1.2$ nm) [24] and WTe₂/HOPG ($h = 1.2 \pm 0.1$ nm) (this work) suggests a smaller van der Waals gap, resulting in stronger interlayer coupling and hybridization of electronic states.

We observe some variations in the electronic structure across different monolayer crystals, reflecting varying doping levels and the presence of in-gap impurity states around the visible adatom disorder [Figs. 1(a) and 1(b)]. We therefore focus on spectra obtained on clean monolayer regions which display a clear suppression of the LDOS over an energy range of several tens of meV around the Fermi energy, and with signatures of an edge state in the normal state. As shown

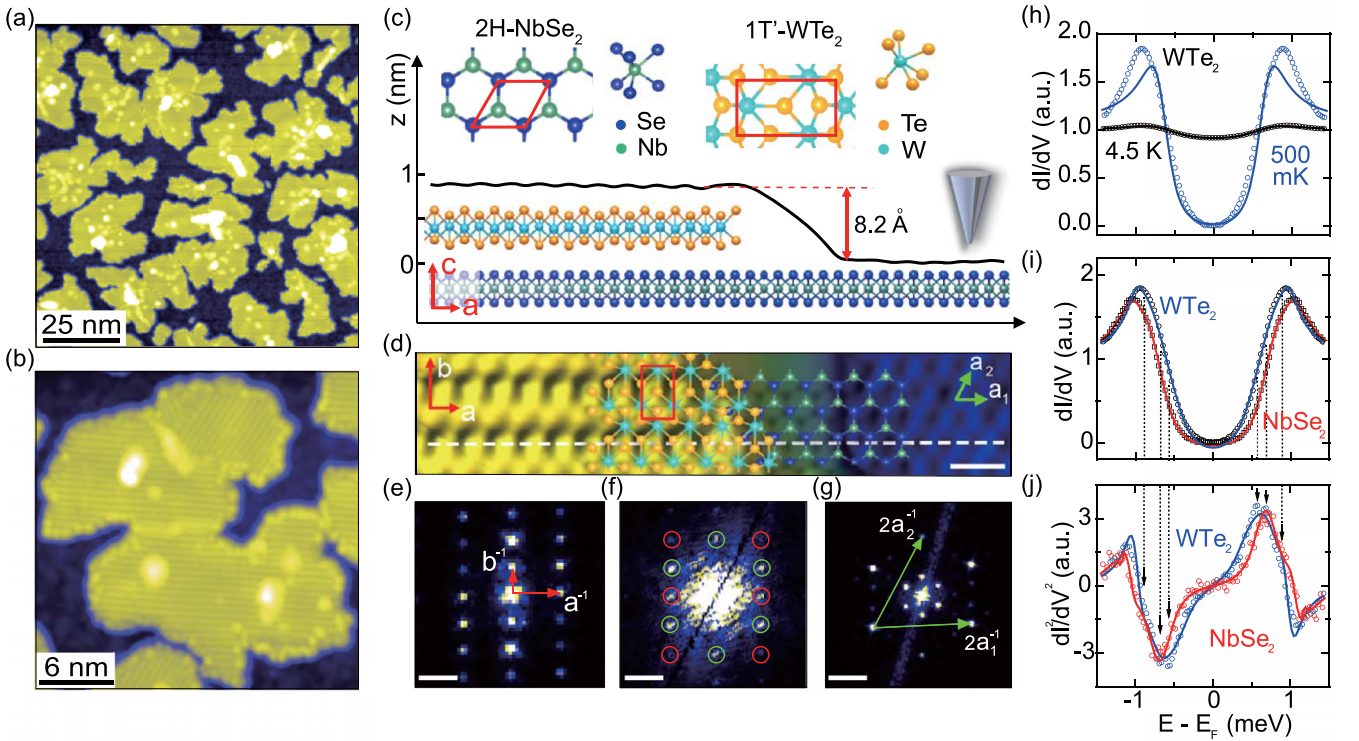


FIG. 1. Superconducting $\text{WTe}_2/\text{NbSe}_2$ heterostructures. (a), (b) STM topography (1.6 V, 100 pA) of monolayer $1T'$ - WTe_2 islands grown on a single crystal of $2H$ - NbSe_2 by van der Waals epitaxy. (c) STM measured height profile corresponding to the dashed white line in panel (d), showing a monolayer height of 8.2 \AA . The inset shows the respective $1T'$ - WTe_2 and $2H$ - NbSe_2 crystal structures. (d) Atomic-resolution close-up (100 mV, 2.2 nA) of the $1T'$ - WTe_2 edge, showing detail of the atomic alignment. The respective chalcogen sublattices are seen to align along the y direction of the $1T'$ - WTe_2 crystal (scale bar: 6.2 \AA). 2D fast Fourier transforms of (e) the $1T'$ - WTe_2 lattice, (f) an area with 46% WTe_2 monolayer coverage, and (g) the pristine NbSe_2 surface after cleaving (all scale bars: 2 nm^{-1}). We estimate $a \simeq a_1 = 3.5 \pm 0.2 \text{ \AA}$, and $b \simeq 2a_2 \cos(30^\circ) = 6.2 \pm 0.3 \text{ \AA}$ for the lattice constants. (h) Temperature dependence of the superconducting local density of states (LDOS) measured in the $\text{WTe}_2/\text{NbSe}_2$ two-dimensional bulk, comparing measurements at $T = 4.5 \text{ K}$ (black) and 500 mK (blue). Solid blue and black lines are fits to a conventional single-band BCS model. (i) High-resolution tunneling spectra, comparing the $\text{WTe}_2/\text{NbSe}_2$ bulk spectrum with that measured on the bare NbSe_2 substrate. Solid red and blue lines are fits to our two-band (NbSe_2) and three-band (WTe_2) McMillan models, respectively (see main text for detail). (j) Second derivative of tunnel current, corresponding to the data shown in panel (i). Dashed lines and arrows indicate the positions of the respective superconducting energy gaps.

in the comparison of Fig. 2 below, such spectra agree well with tight-binding calculations of the normal-state electronic structure, as well as with those published on WTe_2/BLG [23,24,26,27]. Given the metallic nature of the two substrates used in this work, we do not expect that excitonic insulating effects [29,30] play a dominant role here because Coulomb interactions would be expected to be strongly screened.

B. Multiband superconductivity

The clear signature of a superconducting energy gap, measured in the 2D bulk of monolayer WTe_2 , is shown in Figs. 1(h), comparing the superconducting LDOS at 4.5 K with that measured at 500 mK. Fits to conventional BCS theory (solid lines) describe the data well only at 4.5 K but fail to describe the details of the energy gap resolved at 500 mK. This becomes particularly apparent by an underestimation of the width and height of the coherence peaks at $\pm 1 \text{ meV}$. A comparison of high-resolution spectra measured, respectively, on the WTe_2 and NbSe_2 surfaces, is shown in Fig. 1(i). We observe a slightly reduced gap size on NbSe_2 post-MBE growth, compared with the pristine NbSe_2 surface, which is likely due

to a partial quenching of the $3Q$ charge-density wave (CDW) order [40,41] leading to disorder averaging of the Fermi-surface anisotropy and reduced interband coupling (see Fig. 7 and Appendix B for further detail). A further reduction of the superconducting gap measured on $\text{WTe}_2/\text{NbSe}_2$ corroborates that superconductivity is induced into the monolayer via the substrate.

As detailed below, we are able to accurately describe the measured superconducting LDOS within a self-consistent multiband framework based on the McMillan equations [14,41,42] (blue/red lines). In the presence of multiple *noninteracting* bands i , the superconducting density of states can be expressed as a simple sum $N(E) = \sum_i N_i(E)$ of two or more partial densities of states,

$$N_i(E) = \tilde{N}_i(E_F) \text{Re} \left[\frac{|E - i\gamma_i|}{\sqrt{(E - i\gamma_i)^2 - \Delta_i(E)^2}} \right]. \quad (1)$$

Within conventional BCS theory, the order parameter Δ is a constant. The prefactor $\tilde{N}_i(E_F)$ denotes the partial state density of states of band i in the normal state and, in the superconducting state, takes the role [41] of an effective partial

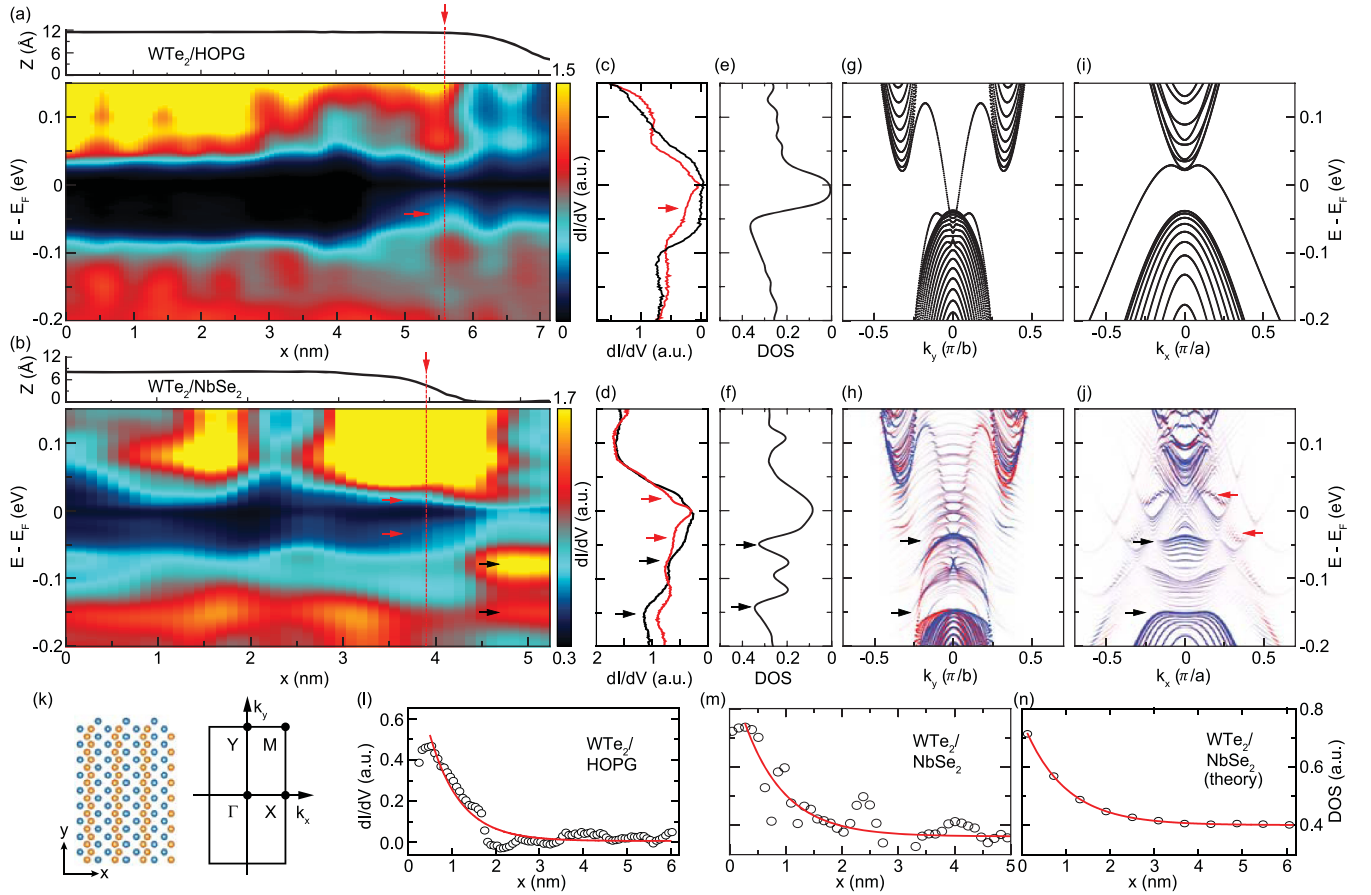


FIG. 2. Hybrid electronic structure of strongly coupled $1T'$ - WTe_2 heterostructures. Spatial profiles of the measured normal-state local density of states (LDOS) across the monolayer edge for (a) WTe_2/HOPG and (b) $\text{WTe}_2/\text{NbSe}_2$, alongside corresponding STM height profiles. (c), (d) individual point spectra of the local density of states (LDOS) in 2D bulk (black) and edge (red), measured at $T = 4.2$ K and compared with tight-binding calculation (e), (f), respectively. (g)–(j) Tight-binding band structures of free-standing WTe_2 monolayers in Γ - Y (g) and Γ - X (i) direction, respectively, and compared with the spin-resolved (blue/red) WTe_2 orbital weight of a $\text{WTe}_2/\text{NbSe}_2$ heterostructure in (h) Γ - Y and (i) Γ - X . The measured LDOS in panels (a) and (b) was taken along the y direction, across the Γ - X edge. Red dashed lines in panels (a) and (b) indicate the positions at which the edge state point spectra in panels (c) and (d) were measured. Black arrows indicate spectral features resolved on $\text{WTe}_2/\text{NbSe}_2$, only, arising from the NbSe_2 substrate. Red arrows indicate the enhanced LDOS at the crystal edges. (k) Lattice model and first Brillouin zone of $1T'$ - WTe_2 , indicating high-symmetry points and directions. (l)–(n) Spatial profiles of the integrated edge-state LDOS (-50 meV to $+20$ meV) for (l) WTe_2/HOPG and (m) $\text{WTe}_2/\text{NbSe}_2$, compared with (n) tight-binding calculations. We define the edge position electronically, where the integrated LDOS peaks and exponentially decays into the 2D bulk gap. Red lines in panels (l)–(n) are exponential fits to extract the edge state decay lengths, $\xi = (0.7 \pm 0.1)$ nm (WTe_2/HOPG), $\xi = (0.7 \pm 0.2)$ nm ($\text{WTe}_2/\text{NbSe}_2$), and $\xi = (1.0 \pm 0.0)$ nm (theory).

density of states weight to the total density of states [Eq. (C3)]. An additional broadening parameter γ_i is usually included to account for energy broadening during the tunneling process (Dynes parameter) [43].

Different from BCS theory, the McMillan model [14] considers *coupled* bands with order parameters $\Delta_i(E)$ that are energy-dependent complex functions of the form

$$\Delta_i(E) = \frac{\Delta_i^0 + \Gamma_{ij}\Delta_j(E)/\sqrt{\Delta_j^2(E) - (E - i\gamma_j)^2}}{1 + \Gamma_{ij}/\sqrt{\Delta_j^2(E) - (E - i\gamma_j)^2}}. \quad (2)$$

Here, an interband Cooper pair tunneling across the van der Waals gap at rate Γ_{ij} renormalizes the intrinsic order parameters of the separate materials Δ_i^0 , leading to a set of

self-consistent equations that can be solved numerically to fit our data.

Although originally developed to describe the superconducting proximity effect in single-band metallic systems, the McMillan model has more recently been successfully applied to describe intrinsic multiband superconductivity in layered two-band superconductors [42], including NbSe_2 [41,44]. For this work, we further extend the McMillan model to describe the hybrid electronic structure of $1T'$ - $\text{WTe}_2/\text{NbSe}_2$ heterostructures, thus treating multiband superconductivity and proximity coupling within the same theoretical framework. To this end, we consider a third order parameter Δ_{WTe_2} , coupled to the NbSe_2 K band (see supporting information), assuming $\Delta_{\text{WTe}_2}^0 = 0$. Fits to both a two-band (NbSe_2 , red line) and a three-band ($\text{WTe}_2/\text{NbSe}_2$, blue line) model describe the data well [Fig. 1(i)] and reproduce the known NbSe_2 order param-

TABLE I. Multiband superconductivity and Fermi-surface anisotropy. Summary of measured NbSe₂ order parameters published in the literature.

Model	Measured gap (meV)	Reference	Experiment
Two band (BCS)	$\Delta_S = 0.50$ $\Delta_L = 1.05$	[39]	STS
	$\Delta_S = 0.73$ $\Delta_L = 1.26$	[38]	Specific heat
	$\Delta_S = 0.85$ $\Delta_L = 1.50$	[57]	Specific heat
	$\Delta_{\min} = 0.65$ $\Delta_{\max} = 1.62$	[57]	Specific heat
Single band (anisotropic)	$\Delta_{\min} = 0.56$ $\Delta_{\max} = 1.30$	[58]	Penetration length
	$\Delta_{\min} = 0.62$ $\Delta_{\max} = 1.30$	[56]	Electron transport
Two band McMillan	$\Delta_S = 0$ $\Delta_L = 1.3$	[41]	STS
	$\Delta_S = 0 - 0.3$ $\Delta_L = 1.26$	[44]	Electron transport
	$\Delta_S = 0.45$ $\Delta_L = 1.10$	This work	STS

eters (see Tables I and II). Indeed, we find that simpler BCS-based models are unable to represent the data well at 500 mK (Appendix B), further confirming the multiband hybrid electronic structure. For the real part of the induced order parameter, we find $\Delta_{\text{WTe}_2}(E_F) = (0.57 \pm 0.02)$ meV, reflecting induced pairing in the strongly coupled heterostructure, in reasonable agreement with recent transport [38] and local probe [39] spectroscopy of nonepitaxial WTe₂/NbSe₂ heterojunctions.

C. Hybrid electronic structure

As inferred from our three-band model, we understand that superconductivity is induced in the WTe₂ bulk as a result of strong interband coupling to the substrate giving rise to a WTe₂/NbSe₂ hybrid electronic structure. We confirm this notion in Fig. 2 by directly comparing spectra of the normal-state LDOS with tight-binding band-structure calculations [45] (Appendix F). In Figs. 2(a) and 2(b) we show the spatial evolution of the measured normal-state LDOS

across a monolayer edge, comparing the WTe₂/HOPG and the WTe₂/NbSe₂ heterostructure, respectively, alongside corresponding height profiles. Individual point spectra of the 2D bulk (black) and 1D edge (red) are furthermore shown in the insets to Figs. 2(c) and 2(d). In both heterostructures, the LDOS shows clear signs of a suppression over $\simeq 70$ meV around the Fermi energy, corresponding to a soft gap. This gap is significantly more developed in WTe₂/HOPG but shows up with comparable magnitude and position also on WTe₂/NbSe₂. A residual 2D bulk LDOS within the gap is measurable on both substrates but is much more pronounced in WTe₂/NbSe₂, attesting to strong hybridization in the heterostructure.

Tight-binding band-structure calculations of a freestanding WTe₂ monolayer are shown in Fig. 2(c) and compared with the spin-resolved WTe₂ orbital weight of the hybridized WTe₂/NbSe₂ heterostructure [Fig. 2(d)]. We find the best agreement for an interlayer hopping of 0.15 eV (see Appendix), similar in magnitude to the Nb-Nb hopping strength within the 2H-NbSe₂ cell [46]. A slightly larger hopping strength would be expected given the shorter Nb-Te separation. The direct comparison with our measured spectra (insets) shows reasonable agreement with regard to the position of the band edges (horizontal dashed lines), the Fermi energy ($E = E_F$), as well as edge state features (red arrows). Indeed, the WTe₂/HOPG spectra resemble closely those previously reported for monolayer WTe₂ grown on bilayer graphene [23,24], indicating that heterostructures with graphitic substrates are only weakly hybridized. The additional spectral features (black arrows), however, only observed in the WTe₂/NbSe₂ heterostructure, need to be attributed the presence of a NbSe₂ partial DOS [reference spectrum in the left-hand inset to Fig. 2(d)], confirming the hybridization picture.

As a result of the strong hybridization in WTe₂/NbSe₂, we further observe a substantial weakening of the topological edge state signature compared with our observations on WTe₂/HOPG and WTe₂/BLG [23,24,26,27]. This is illustrated in Figs. 2(e)–2(g) by plotting spatial profiles of the integrated LDOS within the gap (-50 meV and $+20$ meV) away from the edge position. We extract roughly consistent exponential decay lengths of ≈ 1 nm for both heterostructures. However, the ratio of the edge state LDOS to that in the bulk is much lower for WTe₂/NbSe₂ ($\simeq 1.8$) compared with WTe₂/HOPG ($\simeq 10$) given the large residual LDOS in the bulk gap. Both edge state decay length and LDOS ratio agree well with our tight-binding calculations of the hybrid electronic structure for WTe₂/NbSe₂, as shown in Fig. 2(g).

TABLE II. Consistency across two-band and three-band McMillan models when describing NbSe₂ substrate and WTe₂/NbSe₂ heterostructures, respectively.

Band i	Model	Δ_i^0 (meV)	$\Delta_i(E_F)$ (meV)	$\frac{N_S}{N_L}$	$\frac{N_{\text{WTe}_2}}{N_L}$	$\tilde{N}_i(E_F)$
$i = L$ (Nb K point)	3 band	1.13 ± 0.05	0.87 ± 0.05			0.002 ± 0.001
	2 band	1.11 ± 0.05	1.00 ± 0.05			
$i = S$ (Nb Γ point)	3 band	0.43 ± 0.08	0.68 ± 0.08	0.36 ± 0.03		0.30 ± 0.08
	2 band	0.45 ± 0.09	0.73 ± 0.09	0.36 ± 0.01		
$i = 3$ (WTe ₂)	3 band	0	0.58 ± 0.02		0.19 ± 0.01	0.69 ± 0.06
	2 band					

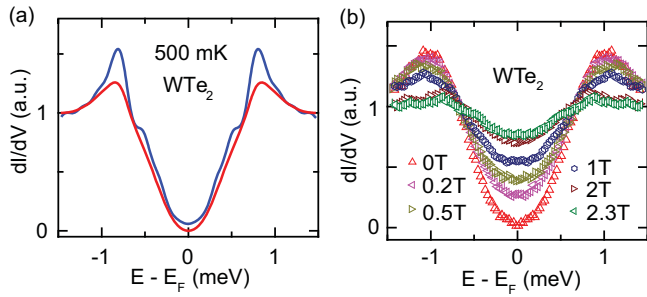


FIG. 3. Magnetic-field dependence of the $\text{WTe}_2/\text{NbSe}_2$ superconducting local density of states (LDOS). (a) Calculated LDOS at 500 mK for an interlayer coupling of 0.15 eV with (red) and without (blue) energy broadening (0.15 meV) included. (b) Magnetic-field dependence of the measured superconducting LDOS up to $B = 2.3$ T, with magnetic field applied perpendicular to the heterostructure (c axis).

In Fig. 3, we plot the calculated superconducting LDOS for the same interlayer hopping (0.15 eV) as used for both the band-structure calculation in Fig. 2(d) and the LDOS profile in Fig. 2(g). We extract $\Delta = 0.58$ meV on the top-most tellurium sublattice, which the STM is expected to be most sensitive to, in remarkable agreement with experiment [$\Delta_{\text{WTe}_2}(E_F) = (0.57 \pm 0.02)$ meV], as extracted from our three-band fits.

The magnetic-field stability of superconducting pairing in the WTe_2 monolayer bulk is investigated in Fig. 3(b), where we plot the measured superconducting LDOS for magnetic fields up to $B = 2.3$ T applied perpendicular to the sample plane (c axis).

D. Spatial profile at the monolayer edge

In Fig. 4, we investigate the spatial evolution of the superconducting LDOS across the WTe_2 monolayer edge. An atomic resolution STM image of a clean WTe_2 edge is shown in Fig. 4(a), indicating position and direction of the STM height profile. The spatial dependence of the superconducting energy gap, measured at 500 mK, is shown Fig. 4(b), alongside the superconducting partial density of states weight $\tilde{N}_i(E, E_F)$ of the $\text{WTe}_2/\text{NbSe}_2$ heterostructure [Fig. 4(c)]. The latter has been extracted self-consistently, using Eqs. (1) and (D1). We observe a pronounced crossover in the partial density of states at ($x_0 \simeq 5.3$ nm), coinciding with the edge position, beyond which the WTe_2 DOS drops to zero as the STM tip leaves the monolayer crystal. In the monolayer bulk, we find that WTe_2 dominates the total DOS with $(63 \pm 5)\%$, with a contribution of $(37 \pm 5)\%$ by the NbSe_2 substrate partial DOS. Interestingly, a more pronounced enhancement in the superconducting partial DOS at the edge appears absent, at least when compared with the normal-state DOS in Fig. 2(f). This is likely due to the vanishing total LDOS at the edge at $E - E_F \simeq 0$ seen in the normal state [compare red curves in Figs. 2(c) and 2(d)], possibly due to the presence of an interaction-driven pseudogap [23,47–49].

A further confirmation of three-band superconductivity is given in Fig. 4(d) where we plot the spatial profile of the second derivative of the tunneling current for energies close to the coherence peak. We observe a sharp transition from

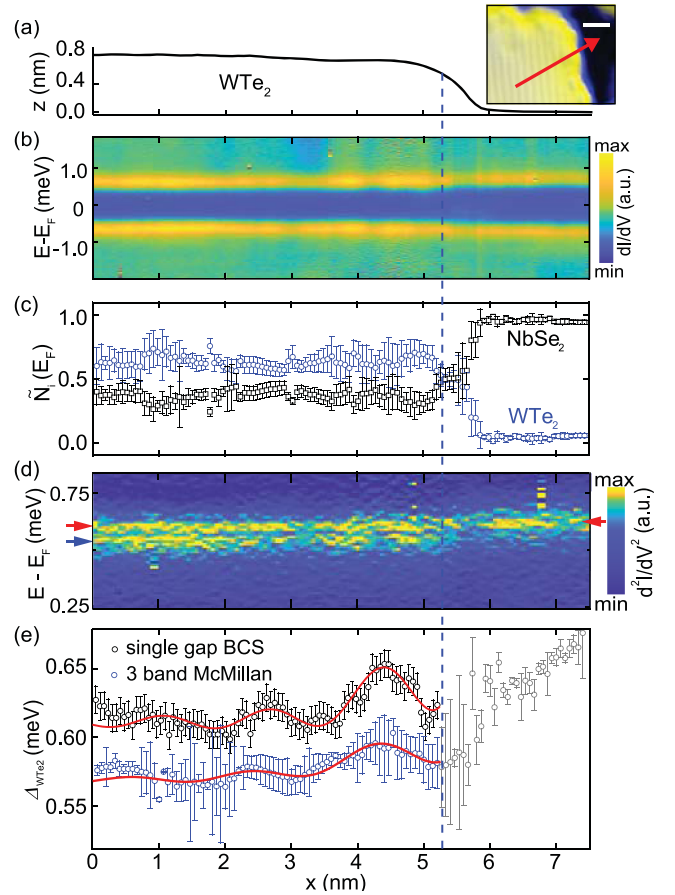


FIG. 4. Multiband superconductivity at the WTe_2 monolayer edge. (a) STM-height profile measured across a clean edge of a WTe_2 monolayer crystal. The inset shows the corresponding STM topograph indicating position and direction of the line profile (red arrow). (b) A series of tunneling spectra measured $T = 500$ mK for points across the edge. (c) The partial density of states weight $\tilde{N}_i(E_F)$, extracted from our three-band analysis in panel (b), shows a clear crossover at the edge $x_0 \simeq 5.3$ nm (dashed line) beyond which the WTe_2 partial density of states vanishes. (d) The second derivative of the tunnel current close to the coherence peaks shows clear signatures of three-band superconductivity. (e) Extracted spatial profile of the induced order parameter $\Delta_{\text{WTe}_2}(x)$ (blue), compared with a single-band BCS-Dynes model (black). Solid red lines are fits to Eq. (3).

two-band to three-band signatures as soon as the probe tip crosses the monolayer edge (dashed line). Arrows indicate the gap energies for the WTe_2 induced gap (blue) and the intrinsic NbSe_2 small gap (red). The NbSe_2 large gap at higher energy is not seen here but is indicated in Figs. 8(a) and 8(b) of the Appendix.

A spatial profile of the extracted order parameter $\Delta_{\text{WTe}_2}(x)$ is shown in Fig. 4(e) in which we observe spatial oscillations with a period of $\simeq 2$ nm. Oscillations of comparable period are also observed in the order parameter extracted from a simple single-band BCS model, and are visible in the energy-integrated normal-state LDOS [Fig. 2(f)]. This suggests that these arise from Friedel-like oscillations in the local density of states due to scattering of 2D bulk states at the WTe_2 edge. Indeed, we can fit the extracted order parameter with a simple

empirical model,

$$\Delta(x) = \frac{A \sin [2k_F(x - x_0)]}{(x - x_0)} + B \exp\left(\frac{x - x_0}{\xi}\right) + C, \quad (3)$$

in which the first term reflects the oscillatory behavior in the local order parameter due to quasiparticle-interference in the 2D bulk. The second term accounts for a residual enhancement of the exponentially decaying 1D edge state, with decay length $\xi = (1.1 \pm 0.2)$ nm comparable to our measurements of the normal-state LDOS [Fig. 2(g)]. The simple model thus simultaneously confirms the edge position ($x_0 = 5.3$ nm) and the Fermi wave vector [50] $k_F \simeq 1.8$ nm⁻¹, and the edge state decay length. Upon crossing the edge, $\Delta_{\text{WTe}_2}(E_F)$ increases to approach the smaller of the two renormalized order parameters of NbSe₂ [$\Delta_S(E_F) = 0.68 \pm 0.08$ meV] as the three-band model emulates the two-band superconductivity of the substrate. This transition coincides with a vanishing WTe₂ partial DOS, which confirms that the grayed-out data points in Fig. 4(e) do not contribute any significant spectral weight to the overall measured density of states.

III. CONCLUSIONS

In summary, we have reported signatures of multiband superconductivity in strongly coupled 1T'-WTe₂/NbSe₂ heterostructures grown by van der Waals epitaxy. By analyzing the superconducting density of states down to 500 mK in scanning probe spectroscopy, we have shown that strong hybridization of electronic states gives rise to a semimetallic density of states in the 2D bulk even in nominally-band-insulating crystals. Describing the detailed functional form of the superconducting energy gap in a self-consistent multiband framework based on the McMillan equations, we confirm the strong interband coupling. Our quantitative comparison of the measured local density of states with a material-specific tight-binding model ultimately confirms the hybrid electronic structure, in both normal and superconducting states for the same interlayer hopping, thus accurately predicting the magnitude of the induced WTe₂ order parameter, $\Delta_{\text{WTe}_2}(B = 0) \simeq 0.55$ meV, stable beyond a 2 T magnetic field. Despite the strong hybridization, we find that a measurable enhancement of the measured local density of states persists at the crystal edges, detectable in both the normal state and in a slight enhancement of the order parameter in the superconducting state. We believe that our multiband treatment of strongly hybridized van der Waals heterostructures will form a useful tool to mapping spatial variation of the induced superconducting order parameter in a wider range of proximitized atomically thin topological materials [51].

ACKNOWLEDGMENTS

This research is supported by National Research Foundation (NRF) Singapore, under the Competitive Research Programme ‘‘Towards On-Chip Topological Quantum Devices’’ (NRF-CRP21-2018-0001), with partial support from a Singapore Ministry of Education (MOE) Academic Research Fund Tier 3 grant (MOE2018-T3-1-002). The work was supported in part by Grants-in-Aid for Scientific Research from the Japan Society for the Promotion of Science

(Grants No. 16H02109, No. 18K19013, and No. 19H00859). The work at Northeastern University was supported by the US Department of Energy (DOE), Office of Science, Basic Energy Sciences grant number DE-SC0019275 and benefited from Northeastern University’s Advanced Scientific Computation Center (ASCC) and the NERSC supercomputing center through DOE Grant No. DE-AC02-05CH11231. K.E.J.G. acknowledges support from the Agency for Science, Technology and Research (A*STAR) under its A*STAR QTE Grant No. A1685b0005. H.L. acknowledges support by the Ministry of Science and Technology (MOST) in Taiwan under Grant No. MOST 109-2112-M-001-014-MY3. S.M. would like to acknowledge the new faculty seed grant from IIT Madras under project number Project No: PHY/18-19/703/NFSC/SHAA. B.W. acknowledges a Singapore National Research Foundation (NRF) Fellowship (NRF-NRFF2017-11). We thank Jack T. Hellerstedt for technical advice during the early stages of crystal growth.

APPENDIX A: 1T'-WTe₂ CRYSTAL GROWTH

van der Waals molecular-beam epitaxy (MBE) was performed in an Omicron Lab10 MBE (base pressure 2×10^{-10} mBar) on bulk crystals of 2H-NbSe₂ (HQ graphene, Netherlands) and highly oriented pyrolytic graphite (HOPG). The substrates were mechanically cleaved in ultrahigh vacuum (UHV) after degassing overnight (300° C), following co-deposition of W (99.998%) and Te (99.999%) for approximately 1 h at a Te : W flux ratio of roughly 260 : 1. We use slightly different substrate temperatures for the two heterostructures with 145° C for 1T'-WTe₂/NbSe₂, and 230° C for 1T'-WTe₂/HOPG. Typical STM images of the WTe₂/HOPG and WTe₂/NbSe₂ heterostructures, respectively, are shown in Figs. 5(a) and 5(b), alongside measurements of the respective WTe₂ monolayer height, extracted from *z*-height histograms 5(c) and 5(d).

APPENDIX B: ELECTRONIC STRUCTURE AND SUPERCONDUCTIVITY OF NbSe₂

NbSe₂ is a type-II superconductor [52,53] with a critical temperature $T_C = 7.2$ K and field $B_{C2} \sim 5$ T [54,55]. The microscopic detail of its superconductivity has been investigated intensively, both theoretically and experimentally [36,40,41,56].

The NbSe₂ Fermi surface [46,59,60] is composed of at least two bands at the Fermi energy. Tight-binding calculations of the NbSe₂ low-energy band structure are shown in Fig. 6, where the black and red lines are bands due to the $d_{3z^2-r^2}$ orbitals centered on the two Nb atoms within the unit cell (Nb bands). These form bonding and antibonding orbitals, giving rise to cylinders at the six *K* points of the hexagonal Brillouin zone. A third band (predominantly Se) [40] has been neglected in our model because it is not believed to contribute to multiband superconductivity in NbSe₂ [40]. As a result of the two-band nature, two distinct superconducting energy gaps, Δ_L and Δ_S , are usually observed at very low temperatures ($T \ll T_C$) [38,41,57] (see Table I), each hosted within the two Nb bands [40,41,44]. Superconducting pairing is significantly stronger in the Nb *K* bands [36,40,41], giving

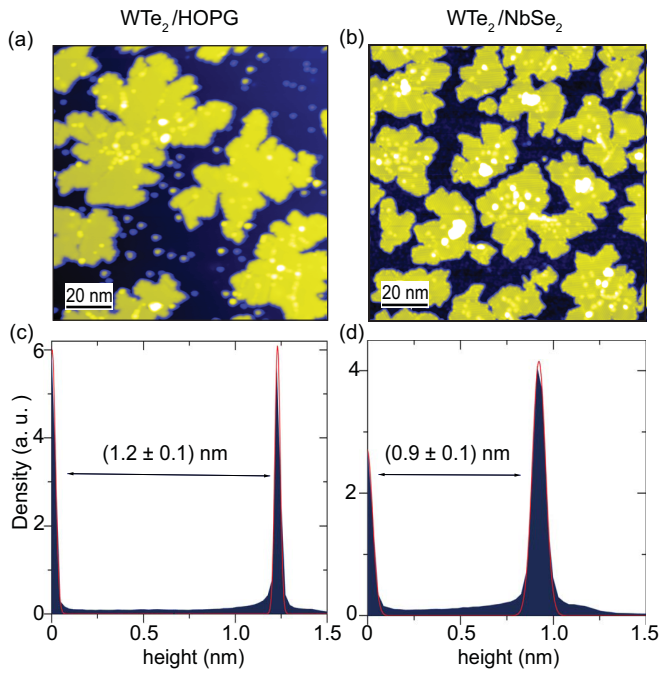


FIG. 5. Height estimates for monolayer WTe_2 islands on different substrates. Large-scale STM topography images, showing a number of $1T'$ - WTe_2 islands, respectively, on (a) HOPG and on (b) NbSe_2 substrates. (c), (d) Corresponding histograms of the z -height information extracted. Fits to a normal distribution (red lines) allow us to estimate the monolayer height (1.2 ± 0.1) nm (WTe_2/HOPG) and (0.9 ± 0.1) nm ($\text{WTe}_2/\text{NbSe}_2$), respectively.

rise to the larger of the two gaps $\Delta_L \simeq 1.3$ meV. At Γ , the pairing is weaker with order parameter Δ_S and is usually found to range between zero and 0.3 meV [36,41].

CDW order on the pristine NbSe_2 surface also plays an important role in scanning tunneling microscopy measurements of the superconducting gap. In pristine NbSe_2 , the $3Q$ charge-density wave (CDW) gives rise to an anisotropic Fermi surface and a reduced Brillouin zone with hexagonal symmetry [41]. Possible mechanism for a suppression of T_C have been argued to result from a reduction of the highly anisotropic superconducting gap due to disorder averaging and/or from the suppression of assistive short-range CDW correlations [61]. From a multiband perspective, the CDW

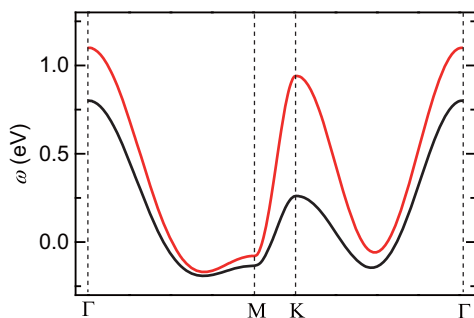


FIG. 6. Tight-binding calculation of the low-energy NbSe_2 band structure. The black and red lines show bands arising from the $d_{3z^2-r^2}$ orbitals centered on the two Nb atoms within the unit cell.

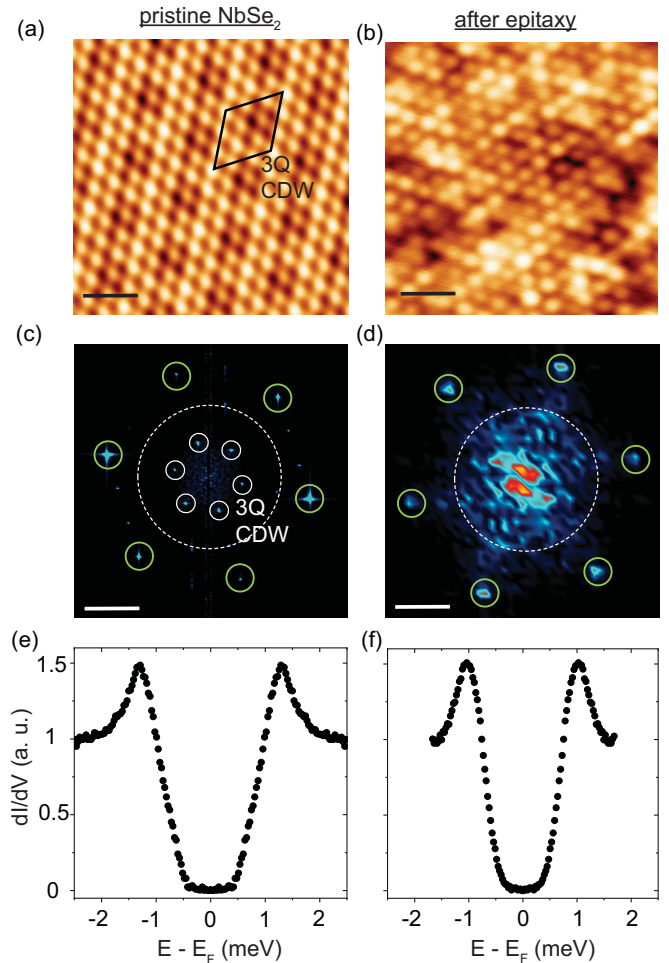


FIG. 7. Quenching of charge-density wave (CDW) order on the NbSe_2 surface postepitaxy. STM images of (a) pristine NbSe_2 surface after cleaving in UHV, and (b) following epitaxy of a submonolayer coverage of WTe_2 . Corresponding fast Fourier transforms show that clear signatures of the (c) $3Q$ CDW wave vector cannot be discerned (d) postepitaxy. Corresponding measured local density of states, measured (e) before and (f) after epitaxy, showing a slight reduction and rounding of the superconducting energy gap.

wave vectors $g_{i,\text{CDW}} = 1/3G_i$ link states at the Γ point (associated with the NbSe_2 small gap) to the Nb cylinders at K (associated with the large gap). This allows for the observation of the large gap on pristine NbSe_2 surfaces in scanning tunneling experiments [40,41], which are most sensitive to states at Γ (tunnelling of electrons with finite transverse momentum is strongly suppressed in STM due to the vertical tunneling path). Once CDW order is suppressed, STM will predominantly probe states at Γ , which would explain the reduced gap observed [41]. Figure 7 shows a comparison of the measured gap on both the pristine and the postgrowth NbSe_2 surface, with a reduction in gap size clearly visible.

APPENDIX C: COMPARISON OF DIFFERENT MODELS FOR THE SUPERCONDUCTING DENSITY OF STATES

Low-temperature scanning tunneling spectroscopy (STM/STS) measurements were carried out in an Omicron

low-temperature STM (junction temperature $T \simeq 4.5$ K) and a Unisoku USM1300 He-3 STM (junction temperature $T \simeq 500$ mK), respectively. Spectroscopic measurements were obtained by using standard lock-in techniques, with an AC excitation of amplitude of 1.5 mV at 831 Hz for measurements of the normal-state electronic structure, and 60 μ V at 931 Hz for measurements in the superconducting state. In all measurements, we fix the current set point 200 pA at 10 mV, ahead of spectroscopy. All spectra of superconducting states through the paper have been spatially averaged, symmetrized about zero bias, and normalized with respect to the normal-state conductance, unless otherwise specified.

In the limit of low bias and low temperature ($k_B T \approx eV$), the tunneling differential conductance, measured by scanning probe spectroscopy, is usually expressed as a convolution of the tunneling density of states $N(E)$ and the derivative of the Fermi-Dirac distribution,

$$dI/dV \propto \int_{-\infty}^{+\infty} \frac{df(E - eV)}{dE} N(E) dE. \quad (\text{C1})$$

For a bulk superconductor with a single isotropic band, a Bardeen-Cooper-Schrieffer (BCS) density of states $N(E) = E/(E^2 - \Delta^2)^{1/2}$ is often assumed and can result in acceptable fits at moderate temperature $T \lesssim T_C$. However, as the derivative of the Fermi-Dirac distribution is a peaked function with half width $\approx 3.5k_B T$, it is responsible for thermal smearing of the measured superconducting tunneling density of states. An additional phenomenological broadening parameter γ (Dynes parameter [43]) is often considered for tunneling experiments,

accounting for additional pair-breaking mechanisms:

$$N(E) = \text{Re} \left[\frac{(E - i\gamma)}{\sqrt{(E - i\gamma)^2 - \Delta^2}} \right]. \quad (\text{C2})$$

At low temperature ($T \ll T_C$), fine detail of the functional form of the superconducting energy gap can be observed [40,44,56]. Indeed, in Fig. 1(h) we see that a BCS-Dynes model provides a good fit only at $T \simeq 4.5$ K but fails to describe the detail of the measured superconducting density of states at lower temperature. A more detailed model is needed to describe the low-temperature data, taking the multiband nature of superconductivity in NbSe₂ into account.

In the presence of multiple (noninteracting) bands i at the Fermi energy, the total tunneling density of states may be expressed as a sum over two or more partial densities of states,

$$N(E) = \sum_i N_i(E) \quad (\text{C3})$$

The partial densities of states can further be expressed as

$$N_i(E) = \tilde{N}_i(E_F) \int_{-\infty}^{\infty} \frac{d\theta}{2\pi} \text{Re} \left[\frac{|E - i\gamma_i|}{\sqrt{(E - i\gamma_i)^2 - \Delta_i(E, \theta)^2}} \right], \quad (\text{C4})$$

where it is assumed that the order parameter $\Delta(E, \theta)$ may not be constant, but itself be a complex energy-dependent and (potentially anisotropic [56]) function. The prefactor, $\tilde{N}_i(E_F) = N_i(E_F)T_i$, can be interpreted [41] as an effective partial density of states weight, renormalized from the true density of states $N_i(E_F)$ by the tunneling probability T_i into band i .

Figure 8 shows a comparison of different models to fit our data, based on Eq. (1), including a single-band BCS-Dynes model ($i = L, \Delta_L$), a two-band BCS-Dynes model ($i = L, S, \Delta_{L,S}$), and an anisotropic single-band model ($i = 1$). The

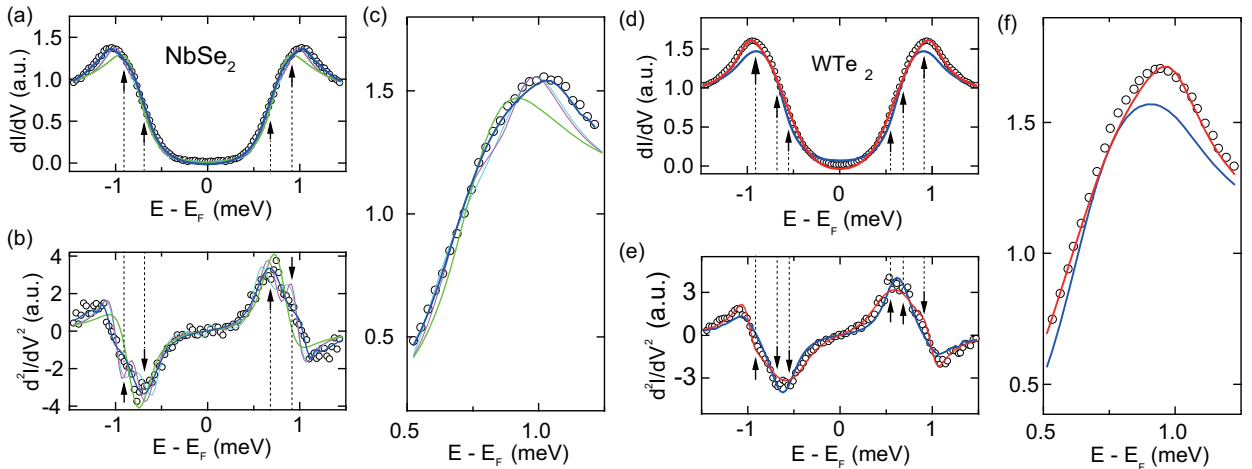


FIG. 8. High-resolution STS spectra of the NbSe₂ and WTe₂ superconducting gaps at 500 mK, comparing different models. (a) Superconducting energy gap of NbSe₂. Solid lines are fits, comparing a single-band BCS-Dynes model (green line), a single anisotropic band model (cyan line), a two-band BCS-Dynes model (magenta line), and a two-band McMillan model (solid blue line). (b), (c) Corresponding second derivative of the tunneling current (d^2I/dV^2) and detail of the coherence peaks. (d)–(f) Superconducting energy gap of WTe₂, comparing a two-band McMillan model (solid blue line) and a three-band McMillan model (solid red line). Panels (e) and (f) are the same as panels (b) and (c). We observe that a two-band McMillan model is insufficient to describe induced superconductivity in WTe₂/NbSe₂. All spectra shown have been spatially averaged, symmetrized about zero bias and normalized with respect to the normal-state conductance. Vertical arrows and dashed lines indicate the renormalized and induced gaps, as determined from the two-band and three-band McMillan models, respectively. Across all models, we find Dynes parameters ranging from 0.02 to 0.1 meV.

second derivative of the tunneling current and close-ups of the coherence peaks are shown alongside to clarify differences in the models. For the anisotropic model we have assumed an empirical anisotropy function, as previously employed for NbSe₂ [56], reflecting the sixfold symmetry of the NbSe₂ Fermi surface,

$$\Delta(A, \theta) = \Delta_0[A \cos(6\theta) + (1 - A)]. \quad (\text{C5})$$

Among the different models, only the two-band BCS and the anisotropic band model provide a somewhat satisfying fit to the measured NbSe₂ data [56]. All models, including the anisotropic band fit underestimate the width of the coherence peaks [Fig. 8(c)].

APPENDIX D: MCMILLAN MODEL

Taking the multiband nature of superconductivity in NbSe₂ into account, a compelling model to describe the superconducting density of states was employed by Noat *et al.* [41] based on the McMillan equations [14]. The McMillan model was originally developed to describe superconductivity between two proximity-coupled materials $i = 1, 2$ in which the intrinsic order parameters Δ_i^0 are renormalized by an interlayer electronic coupling of strength Γ_{ij} . In the context of multiband superconductivity [40–42], the interlayer coupling has since been interpreted as an interband scattering rate from band i to band j (“proximity-effect in reciprocal space”). Different from the other models discussed above, the order parameter $\Delta_i(E)$ in the McMillan model is a complex, energy-dependent gap function:

$$\Delta_i(E) = \frac{\Delta_i^0 + \Gamma_{ij}\Delta_j(E)/\sqrt{\Delta_j(E)^2 - (E - i\gamma_j)^2}}{1 + \Gamma_{ij}/\sqrt{\Delta_j(E)^2 - (E - i\gamma_j)^2}}. \quad (\text{D1})$$

Inclusion of these order parameters in Eq. (1) gives rise to a set of self-consistent equations to describe the multiband system, which can be solved numerically to fit the measured tunneling spectra.

As highlighted in Ref. [41], in addition to the directly measured partial density of states [Eq. (1)], and independent estimate of the partial densities of states ratio at the Fermi energy, $\frac{N_j(E_F)}{N_i(E_F)} = \frac{\Gamma_{ij}}{\Gamma_{ji}}$, can be obtained from a ratio of the interband coupling parameters. Simultaneous extraction of both during the self-consistent numerical fits thus allows for an accurate extraction.

To describe multiband superconductivity in the hybrid WTe₂/NbSe₂ heterostructure, we consider a third order parameter $i = 3$ in Eq. (1). To limit the number of free parameters, we consider coupling $\Gamma_{13(31)}$ only between WTe₂ and the Nb K band (large gap Δ_L^0), which is expected to have the strongest contribution to the proximity coupling [41], and fix $\Gamma_{23(32)} = 0$. We further assume that WTe₂ does not carry any intrinsic superconductivity, such that $\Delta_{\text{WTe}_2}^0 = 0$. Finally, all NbSe₂ related parameters—determined independently from two-band fits to the substrate—can be fixed in the three-band model, in particular, $\Delta_{L,S}^0$ and $\Gamma_{12(21)}$, leaving only three independent fitting parameters in the three-band model.

Figures 8(d)–8(f) show a comparison our three-band McMillan model (solid red line) and the previous two-

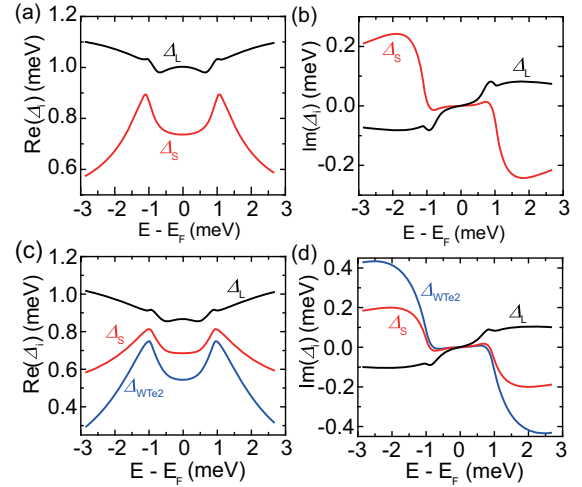


FIG. 9. Energy-dependent order parameters of NbSe₂ and mono-layer 1T'-WTe₂. (a) Real and (b) imaginary parts of the renormalized NbSe₂ order parameters, extracted from a two-band McMillan model. (c), (d) Order parameters of 1T'-WTe₂/NbSe₂, extracted from our three-band McMillan model. Δ_{WTe_2} denotes the induced order parameter.

band model (solid blue line), applied to the WTe₂/NbSe₂ heterostructure. Importantly, a two-band model cannot represent the data well. From the three band model of the heterostructure, we are able to extract the intrinsic NbSe₂ order parameters $\Delta_L^0 = 1.13 \pm 0.05$ meV and $\Delta_S^0 = 0.43 \pm 0.08$ meV, in excellent agreement those extracted from the two-band model of NbSe₂ [41,44]. Consistency of the NbSe₂ order parameter, extracted separately from two-band and three-band models, confirm that the properties of the NbSe₂ parent superconductor remain unaffected by the presence of the WTe₂ epilayer. The renormalized complex order parameters extracted from the three-band fits are plotted in Figs. 9(c) and 9(d). Here, we observe only a minor rebalancing of the interband tunneling rates Γ_{ij} with a concomitant small decrease in the $\text{Re}[\Delta_{L,S}(E_F)]$ as a result of the additional coupling to the third band. The value of the induced order parameter, $\Delta_{\text{WTe}_2}(E_F) = 0.58 \pm 0.02$ meV agrees well with recent local probe [39] and transport spectroscopy [38] of nonepitaxial heterostructures.

APPENDIX E: MEAN-FIELD THEORETICAL MODELLING OF THE HYBRID BAND STRUCTURE

The 1T'-WTe₂/2H-NbSe₂ heterostructure was modeled using a real-space mean-field tight-binding Hamiltonian that is solved using a Bogoliubov-De Gennes (BdG) formalism. The Hamiltonian contains four separate parts given by

$$H = H_N^0 + H_{SC-N} + H_W^0 + H_{W-N}. \quad (\text{E1})$$

The individual terms of the Hamiltonian are given by

$$H_N^0 = \sum_{ijl'l'\sigma} t_{ij}^{ll'} c_{il\sigma}^\dagger c_{j'l'\sigma} + \text{H.c.},$$

$$H_{SC}^N = \sum_{il} \Delta_{il}^N c_{il\uparrow}^\dagger c_{il\downarrow} + \text{H.c.},$$

$$H_{W-N} = t_{\perp} \sum_{ij\sigma} c_{i2\sigma}^{\dagger} d_{j1\sigma} + \text{H.c.},$$

$$H_0^W = \sum_{\mu, \nu, i, j, \sigma, \sigma'} t_{\mu, \nu, \sigma, \sigma'}^{ij} d_{i\mu, \sigma}^{\dagger} d_{j\nu, \sigma'} + \text{H.c.}$$

In H_0^N , operators ($c_{i\sigma}^{\dagger}$, $c_{i\sigma}$) represent the creation and annihilation operators, respectively, at the site i with a single Nb d_{z^2} orbital contributing per site (see below for details). The layer index $l = (1, 2)$ corresponds to the two layers of 2H-NbSe₂, respectively, taking spin $\sigma = (\uparrow, \downarrow)$ into account. The individual real-space tight-binding hopping matrix elements for 2H-NbSe₂ are generated by a basis transformation to orbital basis from a two-band Hamiltonian that has been studied previously to match ARPES [46] and STM experiments [62] on 2H-NbSe₂.

At temperatures below $T \approx 7.2$ K, pristine NbSe₂ undergoes a transition to a superconducting state. Assuming a dominant conventional s -wave superconducting instability, we calculate the superconducting gap $\Delta_{il}^N = V \langle c_{i\uparrow} c_{i\downarrow} \rangle$ self-consistently at each lattice site by solving the BdG equations. The dominant on-site pairing term V is tuned to generate a superconducting gap of $\Delta \approx 1.1$ eV, in agreement with the experimental results on pristine 2H-NbSe₂ (see Table I and references therein).

The electronic structure of 1T'-WTe₂ is modeled by generating a real-space version of an eight-band Hamiltonian, containing two Te and two W atoms in a rectangular unit cell. As discussed in Refs. [45,63,64], this Hamiltonian corresponds to a dominant contribution from Te p_x orbitals, and W $d_{x^2-y^2}$ orbitals, which dominate the low-energy band structure owing to the distorted lattice structure in monolayer 1T'-WTe₂.

In H_0^W , the indices i, j refer to the unit cell, and $\mu, \nu = (1, 2, 3, 4)$ represent the atoms or orbitals within each unit cell. The model provides reasonable agreement with the low-energy electronic structure including the QSH insulator observed in ARPES and STM experiments [23]. In the enclosed additional supplementary files, we provide the real-space hopping matrix elements including the Rashba spin-orbit-coupling terms included in the real-space Hamiltonian for 1T'-WTe₂. The monolayer edge was modeled using an open boundary condition and has been studied for various terminations for directions perpendicular and parallel to the direction of the atomic chains. We find that, although the modeling of the edge with open boundary conditions is simplistic (the edge in as as-grown real material is rough with no consistent termination), the obtained local density of states shows reasonable agreement with the experiments (see Fig. 2 of the main text).

To represent a finite electronic interlayer coupling in the heterostructure, we assume a nearest-neighbor hopping t_{\perp} leading to an effective hybridization between the Nb d_{z^2} orbitals and Te p_x orbitals. This gives rise to a residual metallic density of states within the WTe₂ bulk band gap, in reasonable agreement with our experimental observations in both the normal state (see Fig. 2 of the main text) and the superconducting state (see Fig. 3 of the main text). We find the best

agreement with experiments—simultaneously for normal and superconducting state—for $t_{\perp} \approx 0.15$ eV.

The induced superconducting gap on the Te and W atoms has been evaluated self-consistently by calculating the anomalous averages $\Delta_{i\mu}^W \sim \langle d_{i\mu\uparrow}^{\dagger} d_{i\mu\downarrow}^{\dagger} \rangle$, where $\mu = (1, 2, 3, 4)$ represents the two Te and two W atoms in the unit cell and i is the unit-cell index. The calculations involve a Hamiltonian where the electron operators are considered in momentum space for a direction perpendicular to the edge. For an edge along the y direction, the Bogoliubov-de Gennes transformations involve quasi-particle operators,

$$d_{i_x, k_y, \mu \sigma} = \sum_n (u_{i_x, k_y, \mu \sigma}^n \gamma_{n\sigma} - \sigma v_{i_x, k_y, \mu \sigma}^{n*} \gamma_{n\sigma}^{\dagger}), \quad (\text{E2})$$

$$d_{i_x, k_y, \mu \sigma}^{\dagger} = \sum_n (u_{i_x, k_y, \mu \sigma}^{n*} \gamma_{n\sigma}^{\dagger} - \sigma v_{i_x, k_y, \mu \sigma}^n \gamma_{n\sigma}). \quad (\text{E3})$$

Here, $\gamma_{n\sigma}$ are the quasiparticle operators corresponding to state n and u, v are the corresponding amplitudes. Similar transformations also hold for the c operators for NbSe₂.

Diagonalizing the above BdG Hamiltonian, we self-consistently calculate the electron density $n(i_x)$ and superconducting gap at each lattice site for the multi-orbital Hamiltonian. The mean-fields for the electron density would in general be given by

$$n_{i_x, \mu \sigma} = \frac{1}{N_{k_y}} \sum_{k_y, n} |u_{i_x, k_y, \mu \sigma}^n|^2 f(E_n). \quad (\text{E4})$$

Here, $f(E_n)$ is the Fermi function.

As discussed above, the superconducting gap on NbSe₂ has been introduced with a pairing interaction term V . The self-consistent procedure leads to an induced even-parity ($\Delta_{i_x, j_x, \mu}^s$) order parameter on 1T'-WTe₂. The induced superconducting gaps are obtained from the self-consistent solutions by calculating the following anomalous averages,

$$\Delta_{i_x, j_x, \mu}^s = \frac{1}{N_{k_y}} \sum_{n, k_y=0}^{2\pi} [u_{i_x, k_y, \mu \uparrow}^n v_{j_x, k_y, \mu \downarrow}^{n*} + u_{j_x, k_y, \mu \uparrow}^n v_{i_x, k_y, \mu \downarrow}^{n*}] f(E_n).$$

Here, N_{k_y} is the number of k_y divisions which is typically taken to be 30 000 to 60 000 points to achieve high resolution for the small gaps observed in the system.

We see our model as a generalization from the approximation of a superconducting heterostructure by considering pristine WTe₂ with no effect of the proximal superconductor on the WTe₂ band structure, i.e., a heterostructure in which the only effect of the superconductor is to induce a gap on the QSH edges. Instead, our modeling accounts for a realistic finite interlayer coupling between NbSe₂ and WTe₂ through a self-consistent procedure, allowing for minor changes in the electronic structure such as hybridization and charge transfer. Our model is thus able to explain, simultaneously, a small but finite metallic density of states within the QSH gap, which leaves the edge state intact, and an induced superconducting order parameter of the same magnitude as resolved in the experiments.

- [1] L. Fu and C. L. Kane, Superconducting Proximity Effect and Majorana Fermions at the Surface of a Topological Insulator, *Phys. Rev. Lett.* **100**, 096407 (2008).
- [2] J. Alicea, New directions in the pursuit of Majorana fermions in solid state systems, *Rep. Prog. Phys.* **75**, 076501 (2012).
- [3] C. Beenakker, Search for Majorana fermions in superconductors, *Annu. Rev. Condens. Matter Phys.* **4**, 113 (2013).
- [4] V. Mourik, K. Zuo, S. M. Frolov, S. Plissard, E. P. Bakkers, and L. P. Kouwenhoven, Signatures of Majorana Fermions in hybrid superconductor-semiconductor nanowire devices, *Science* **336**, 1003 (2012).
- [5] S. Nadj-Perge, I. K. Drozdov, J. Li, H. Chen, S. Jeon, J. Seo, A. H. MacDonald, B. A. Bernevig, and A. Yazdani, Observation of Majorana fermions in ferromagnetic atomic chains on a superconductor, *Science* **346**, 602 (2014).
- [6] A. Palacio-Morales, E. Mascot, S. Cocklin, H. Kim, S. Rachel, D. K. Morr, and R. Wiesendanger, Atomic-scale interface engineering of Majorana edge modes in a 2D magnet-superconductor hybrid system, *Sci. Adv.* **5**, eaav6600 (2019).
- [7] H.-H. Sun, K.-W. Zhang, L.-H. Hu, C. Li, G.-Y. Wang, H.-Y. Ma, Z.-A. Xu, C.-L. Gao, D.-D. Guan, Y.-Y. Li, C. Liu, D. Qian, Y. Zhou, L. Fu, S.-C. Li, F.-C. Zhang, and J.-F. Jia, Majorana Zero Mode Detected with Spin Selective Andreev Reflection in the Vortex of a Topological Superconductor, *Phys. Rev. Lett.* **116**, 257003 (2016).
- [8] B. Jäck, Y. Xie, J. Li, S. Jeon, B. A. Bernevig, and A. Yazdani, Observation of a Majorana zero mode in a topologically protected edge channel, *Science* **364**, 1255 (2019).
- [9] L. Fu and C. L. Kane, Probing Neutral Majorana Fermion Edge Modes with Charge Transport, *Phys. Rev. Lett.* **102**, 216403 (2009).
- [10] L. Fu and C. L. Kane, Josephson current and noise at a superconductor/quantum-spin-Hall-insulator/superconductor junction, *Phys. Rev. B* **79**, 161408(R) (2009).
- [11] C. L. Kane and E. J. Mele, Quantum Spin Hall Effect in Graphene, *Phys. Rev. Lett.* **95**, 226801 (2005).
- [12] C. P. Orth, R. P. Tiwari, T. Meng, and T. L. Schmidt, Non-Abelian parafermions in time-reversal-invariant interacting helical systems, *Phys. Rev. B* **91**, 081406(R) (2015).
- [13] D. J. Trainer, B. Wang, F. Bobba, N. Samuelson, X. Xi, J. Zasadzinski, J. Nieminen, A. Bansil, and M. Iavarone, Proximity-induced superconductivity in monolayer MoS₂, *ACS Nano* **14**, 2718 (2020).
- [14] W. McMillan, Tunneling model of the superconducting proximity effect, *Phys. Rev.* **175**, 537 (1968).
- [15] A. A. Soluyanov, D. Gresch, Z. Wang, Q. Wu, M. Troyer, X. Dai, and B. A. Bernevig, Type-II Weyl semimetals, *Nature (London)* **527**, 495 (2015).
- [16] Z. Wang, B. J. Wieder, J. Li, B. Yan, and B. A. Bernevig, Higher-Order Topology, Monopole Nodal Lines, and the Origin of Large Fermi Arcs in Transition Metal Dichalcogenides $x\text{Te}_2$ ($x = \text{Mo}, \text{W}$), *Phys. Rev. Lett.* **123**, 186401 (2019).
- [17] Y.-B. Choi, Y. Xie, C.-Z. Chen, J. Park, S.-B. Song, J. Yoon, B. J. Kim, T. Taniguchi, K. Watanabe, J. Kim, K. C. Fong, M. N. Ali, K. T. Law, and G.-H. Lee, Evidence of higher-order topology in multilayer WTe₂ from Josephson coupling through anisotropic hinge states, *Nat. Mater.* **19**, 974 (2020).
- [18] A. Kononov, G. Abulizi, K. Qu, J. Yan, D. Mandrus, K. Watanabe, T. Taniguchi, and C. Schönberger, One-dimensional edge transport in few-layer WTe₂, *Nano Lett.* **20**, 4228 (2019).
- [19] X. Qian, J. Liu, L. Fu, and J. Li, Quantum spin Hall effect in two-dimensional transition metal dichalcogenides, *Science* **346**, 1344 (2014).
- [20] F. Zheng, C. Cai, S. Ge, X. Zhang, X. Liu, H. Lu, Y. Zhang, J. Qiu, T. Taniguchi, K. Watanabe, S. Jia, J. Qi, J.-H. Chen, D. Sun, and J. Feng, On the quantum spin Hall gap of monolayer WTe₂, *Adv. Mater.* **28**, 4845 (2016).
- [21] Z. Fei, T. Palomaki, S. Wu, W. Zhao, X. Cai, B. Sun, P. Nguyen, J. Finney, X. Xu, and D. H. Cobden, Edge conduction in monolayer WTe₂, *Nat. Phys.* **13**, 677 (2017).
- [22] S. Wu, V. Fatemi, Q. D. Gibson, K. Watanabe, T. Taniguchi, R. J. Cava, and P. Jarillo-Herrero, Observation of the quantum spin Hall effect up to 100 Kelvin in a monolayer crystal, *Science* **359**, 76 (2018).
- [23] S. Tang, C. Zhang, D. Wong, Z. Pedramrazi, H.-Z. Tsai, C. Jia, B. Moritz, M. Claassen, H. Ryu, S. Kahn, J. Jiang, H. Yan, M. Hashimoto, D. Lu, R. G. Moore, C.-C. Hwang, C. Hwang, Z. Hussain, Y. Chen, M. M. Ugeda, Z. Liu, X. Xie, T. P. Devereaux, M. F. Crommie, S.-K. Mo, and Z.-X. Shen, Quantum spin Hall state in monolayer 1T'-WTe₂, *Nat. Phys.* **13**, 683 (2017).
- [24] Z.-Y. Jia, Y.-H. Song, X.-B. Li, K. Ran, P. Lu, H.-J. Zheng, X.-Y. Zhu, Z.-Q. Shi, J. Sun, J. Wen, D. Xing, and S. C. Li, Direct visualization of a two-dimensional topological insulator in the single-layer 1T'-WTe₂, *Phys. Rev. B* **96**, 041108(R) (2017).
- [25] Y. Shi, J. Kahn, B. Niu, Z. Fei, B. Sun, X. Cai, B. A. Francisco, D. Wu, Z.-X. Shen, X. Xu, D. H. Cobden, and Y.-T. Cui, Imaging quantum spin Hall edges in monolayer WTe₂, *Sci. Adv.* **5**, eaat8799 (2019).
- [26] C. Zhao, M. Hu, J. Qin, B. Xia, C. Liu, S. Wang, D. D. Guan, Y. Li, H. Zheng, J. Liu, and J. Jia, Strain Tunable Semimetal-Topological-Insulator Transition in Monolayer 1T'-WTe₂, *Phys. Rev. Lett.* **125**, 046801 (2020).
- [27] Y. Maximenko, Y. Chang, G. Chen, M. R. Hirsbrunner, W. Swiech, T. L. Hughes, L. K. Wagner, and V. Madhavan, Electric field effects on the band gap and edge states of monolayer 1T'-WTe₂, *arXiv:2011.10096*.
- [28] Y.-H. Song, Z.-Y. Jia, D. Zhang, X.-Y. Zhu, Z.-Q. Shi, H. Wang, L. Zhu, Q.-Q. Yuan, H. Zhang, D.-Y. Xing *et al.*, Observation of Coulomb gap in the quantum spin Hall candidate single-layer 1T'-WTe₂, *Nat. Commun.* **9**, 1 (2018).
- [29] P. Wang, G. Yu, Y. Jia, M. Onyszczak, F. A. Cevallos, S. Lei, S. Klemenz, K. Watanabe, T. Taniguchi, R. J. Cava, L. M. Schoop, and S. Wu, Landau quantization and highly mobile fermions in an insulator, *Nature (London)* **589**, 225 (2021).
- [30] Y. Jia, P. Wang, C.-L. Chiu, Z. Song, G. Yu, B. Jäck, S. Lei, S. Klemenz, F. A. Cevallos, M. Onyszczak, N. Fishchenko, X. Liu, G. Farahi, F. Xie, Y. Xu, K. Watanabe, T. Taniguchi, B. A. Bernevig, R. J. Cava, L. M. Schoop, A. Yazdani, and S. Wu, Evidence for a monolayer excitonic insulator, *Nat. Phys.* **18**, 87 (2022).
- [31] F. Zhang and C. L. Kane, Time-Reversal-Invariant Z₄ Fractional Josephson Effect, *Phys. Rev. Lett.* **113**, 036401 (2014).

- [32] Y.-T. Hsu, W. S. Cole, R.-X. Zhang, and J. D. Sau, Inversion-Protected Higher-Order Topological Superconductivity in Monolayer WTe_2 , *Phys. Rev. Lett.* **125**, 097001 (2020).
- [33] V. Crépel and L. Fu, Spin-triplet superconductivity from excitonic effect in doped insulators: Theory and prediction for WTe_2 , [arXiv:2103.12060](https://arxiv.org/abs/2103.12060).
- [34] V. Fatemi, S. Wu, Y. Cao, L. Bretheau, Q. D. Gibson, K. Watanabe, T. Taniguchi, R. J. Cava, and P. Jarillo-Herrero, Electrically tunable low-density superconductivity in a monolayer topological insulator, *Science* **362**, 926 (2018).
- [35] E. Sajadi, T. Palomaki, Z. Fei, W. Zhao, P. Bement, C. Olsen, S. Luescher, X. Xu, J. A. Folk, and D. H. Cobden, Gate-induced superconductivity in a monolayer topological insulator, *Science* **362**, 922 (2018).
- [36] T. Dvir, M. Aprili, C. H. Quay, and H. Steinberg, Tunneling into the vortex state of NbSe_2 with van der Waals junctions, *Nano Lett.* **18**, 7845 (2018).
- [37] Q. Li, C. He, Y. Wang, E. Liu, M. Wang, Y. Wang, J. Zeng, Z. Ma, T. Cao, C. Yi *et al.*, Proximity-induced superconductivity with subgap anomaly in type II Weyl semi-metal WTe_2 , *Nano Lett.* **18**, 7962 (2018).
- [38] C. Huang, A. Narayan, E. Zhang, Y. Liu, X. Yan, J. Wang, C. Zhang, W. Wang, T. Zhou, C. Yi, S. Liu, J. Ling, H. Zhang, R. Liu, R. Sankar, F. Chou, Y. Wang, Y. Shi, K. T. Law, S. Sanvito, P. Zhou, Z. Han, and F. Xiu, Inducing strong superconductivity in WTe_2 by a proximity effect, *ACS Nano* **12**, 7185 (2018).
- [39] F. Lüpke, D. Waters, S. de la Barrera, M. Widom, D. Mandrus, J. Yan, R. Feenstra, and B. Hunt, Proximity-induced superconducting gap in the quantum spin Hall edge state of monolayer WTe_2 , *Nat. Phys.* **16**, 526 (2020).
- [40] Y. Noat, T. Cren, F. Debontridder, D. Roditchev, W. Sacks, P. Toulemonde, and A. San Miguel, Signatures of multigap superconductivity in tunneling spectroscopy, *Phys. Rev. B* **82**, 014531 (2010).
- [41] Y. Noat, J. A. Silva-Guillén, T. Cren, V. Cherkez, C. Brun, S. Pons, F. Debontridder, D. Roditchev, W. Sacks, L. Cario, P. Ordejón, A. García, and E. Canadell, Quasiparticle spectra of 2H-NbSe_2 : Two-band superconductivity and the role of tunneling selectivity, *Phys. Rev. B* **92**, 134510 (2015).
- [42] T. Takasaki, T. Ekino, T. Muranaka, T. Ichikawa, H. Fujii, and J. Akimitsu, Multiple-gap features from break-junction tunneling in the superconducting MgB_2 , *J. Phys. Soc. Jpn.* **73**, 1902 (2004).
- [43] R. C. Dynes, V. Narayanamurti, and J. P. Garno, Direct Measurement of Quasiparticle-Lifetime Broadening in a Strong-Coupled Superconductor, *Phys. Rev. Lett.* **41**, 1509 (1978).
- [44] T. Dvir, F. Masee, L. Attias, M. Khodas, M. Aprili, C. H. Quay, and H. Steinberg, Spectroscopy of bulk and few-layer superconducting NbSe_2 with van der Waals tunnel junctions, *Nat. Commun.* **9**, 1 (2018).
- [45] A. Lau, R. Ray, D. Varjas, and A. R. Akhmerov, Influence of lattice termination on the edge states of the quantum spin Hall insulator monolayer $1T'-\text{WTe}_2$, *Phys. Rev. Materials* **3**, 054206 (2019).
- [46] D. J. Rahn, S. Hellmann, M. Källäne, C. Sohr, T. K. Kim, L. Kipp, and K. Rossnagel, Gaps and kinks in the electronic structure of the superconductor 2H-NbSe_2 from angle-resolved photoemission at 1 K, *Phys. Rev. B* **85**, 224532 (2012).
- [47] R. Stühler, F. Reis, T. Müller, T. Helbig, T. Schwemmer, R. Thomale, J. Schäfer, and R. Claessen, Tomonaga-Luttinger liquid in the edge channels of a quantum spin Hall insulator, *Nat. Phys.* **16**, 47 (2020).
- [48] F. Reis, G. Li, L. Dudy, M. Bauernfeind, S. Glass, W. Hanke, R. Thomale, J. Schäfer, and R. Claessen, Bismuthene on a SiC substrate: A candidate for a high-temperature quantum spin Hall material, *Science* **357**, 287 (2017).
- [49] J. L. Collins, A. Tadich, W. Wu, L. C. Gomes, J. N. Rodrigues, C. Liu, J. Hellerstedt, H. Ryu, S. Tang, S.-K. Mo, S. Adam, S. A. Yang, M. S. Fuhrer, and M. T. Edmonds, Electric-field-tuned topological phase transition in ultrathin Na_3Bi , *Nature (London)* **564**, 390 (2018).
- [50] X.-C. Pan, Y. Pan, J. Jiang, H. Zuo, H. Liu, X. Chen, Z. Wei, S. Zhang, Z. Wang, X. Wan, Z. Yang, D. Feng, Z. Xia, L. Li, F. Song, B. Wang, Y. Zhang, and G. Wang, Carrier balance and linear magnetoresistance in type-II Weyl semimetal WTe_2 , *Front. Phys.* **12**, 127203 (2017).
- [51] M. S. Lodge, S. A. Yang, S. Mukherjee, and B. Weber, Atomically thin quantum spin Hall insulators, *Adv. Mater.* **33**, 2008029 (2021).
- [52] J. A. Wilson, Charge-density waves in the 2H-TaSe_2 family: Action on the Fermi surface, *Phys. Rev. B* **15**, 5748 (1977).
- [53] G. Wexler and A. M. Woolley, Fermi surfaces and band structures of the 2H metallic transition-metal dichalcogenides, *J. Phys. C: Solid State Phys.* **9**, 1185 (1976).
- [54] E. Revolinsky, G. Spiering, and D. Beerntsen, Superconductivity in the niobium-selenium system, *J. Phys. Chem. Solids* **26**, 1029 (1965).
- [55] S. Foner and E. McNiff, Upper critical fields of layered superconducting NbSe_2 at low temperature, *Phys. Lett. A* **45**, 429 (1973).
- [56] E. Khestanova, J. Birkbeck, M. Zhu, Y. Cao, G. Yu, D. Ghazaryan, J. Yin, H. Berger, L. Forro, T. Taniguchi *et al.*, Unusual suppression of the superconducting energy gap and critical temperature in atomically thin NbSe_2 , *Nano Lett.* **18**, 2623 (2018).
- [57] J. Yan, L. Shan, Y. Wang, Z.-L. Xiao, and H.-H. Wen, Quasiparticle density of states of 2H-NbSe_2 single crystals revealed by low-temperature specific heat measurements according to a two-component model, *Chin. Phys. B* **17**, 2229 (2008).
- [58] J. D. Fletcher, A. Carrington, P. Diener, P. Rodière, J. P. Brison, R. Prozorov, T. Olheiser, and R. W. Giannetta, Penetration Depth Study of Superconducting Gap Structure of NbSe_2 , *Phys. Rev. Lett.* **98**, 057003 (2007).
- [59] S. V. Borisenko, A. A. Kordyuk, V. B. Zabolotnyy, D. S. Inosov, D. Evtushinsky, B. Büchner, A. N. Yaresko, A. Varykhalov, R. Follath, W. Eberhardt, L. Patthey, and H. Berger, Two Energy Gaps and Fermi-Surface “Arcs” in NbSe_2 , *Phys. Rev. Lett.* **102**, 166402 (2009).
- [60] T. Yokoya, T. Kiss, A. Chainani, S. Shin, M. Nohara, and H. Takagi, Fermi surface sheet-dependent superconductivity in 2H-NbSe_2 , *Science* **294**, 2518 (2001).
- [61] K. Cho, M. Kończykowski, S. Teknowijoyo, M. A. Tanatar, J. Guss, P. B. Gartin, J. M. Wilde, A. Kreyssig, R. J. McQueeney, A. I. Goldman, V. Mishra, P. J. Hirschfeld, and R. Prozorov, Using controlled disorder to probe the interplay between charge

- order and superconductivity in NbSe₂, [Nat. Commun. **9**, 2796 \(2018\)](#).
- [62] S. Gao, F. Flicker, R. Sankar, H. Zhao, Z. Ren, B. Rachmilowitz, S. Balachandar, F. Chou, K. S. Burch, Z. Wang *et al.*, Atomic-scale strain manipulation of a charge density wave, [Proc. Natl. Acad. Sci. USA **115**, 6986 \(2018\)](#).
- [63] D.-H. Choe, H.-J. Sung, and K. J. Chang, Understanding topological phase transition in monolayer transition metal dichalcogenides, [Phys. Rev. B **93**, 125109 \(2016\)](#).
- [64] L. Muechler, A. Alexandradinata, T. Neupert, and R. Car, Topological Nonsymmorphic Metals from Band Inversion, [Phys. Rev. X **6**, 041069 \(2016\)](#).